

Unified Image and Video Saliency Modeling

Richard Droste*, Jianbo Jiao*, and J. Alison Noble

University of Oxford

{richard.droste, jianbo.jiao, alison.noble}@eng.ox.ac.uk

Abstract. Visual saliency modeling for images and videos is treated as two independent tasks in recent computer vision literature. On the one hand, image saliency modeling is a well-studied problem and progress on benchmarks like SALICON and MIT300 is slowing. For video saliency prediction on the other hand, rapid gains have been achieved on the recent DHF1K benchmark through network architectures that are optimized for this task. Here, we take a step back and ask: Can image and video saliency modeling be approached via a unified model, with mutual benefit? We find that it is crucial to model the domain shift between image and video saliency data and between different video saliency datasets for effective joint modeling. We identify different sources of domain shift and address them through four novel domain adaptation techniques— Domain-Adaptive Priors, Domain-Adaptive Fusion, Domain-Adaptive Smoothing and Bypass-RNN— in addition to an improved formulation of learned Gaussian priors. We integrate these techniques into a simple and lightweight encoder-RNN-decoder-style network, UNISAL, and train the entire network simultaneously with image and video saliency data. We evaluate our method on the video saliency datasets DHF1K, Hollywood-2 and UCF-Sports, as well as the image saliency datasets SALICON and MIT300. With one set of parameters, our method achieves state-of-the-art performance on all video saliency datasets and is on par with the state-of-the-art for image saliency prediction, despite a 5 to 20-fold reduction in model size and the fastest runtime among all competing deep models. We provide retrospective analyses and ablation studies which demonstrate the importance of the domain shift modeling. The code is available at <https://github.com/rdroste/unisal>.

1 Introduction

When processing visual stimuli, humans naturally direct their attention towards informative regions, which can be measured via eye-tracking. The task of predicting the fixation distribution on static scenes (images) and dynamic scenes (videos) is referred to as (*visual*) *saliency prediction/modeling*, and the predicted distributions as *saliency maps*. Convolutional neural networks (CNNs) have emerged as the most performant technique for saliency modeling due to their capacity to learn complex feature hierarchies [2] and the availability of large-scale datasets [20].

Most of the work on saliency modeling focuses on predicting saliency maps on images. In real-life situations, in contrast, humans are usually exposed to dynamic stimuli.

* R. Droste and J. Jiao contributed equally to this work.

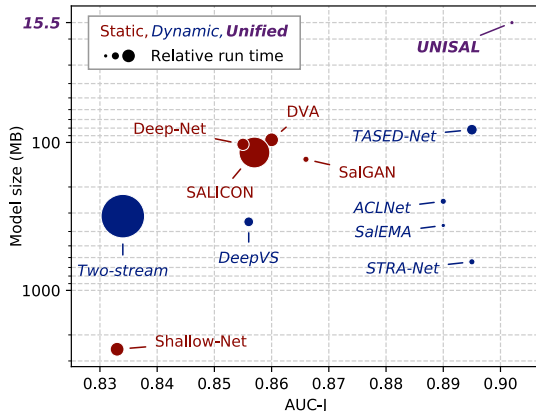


Fig. 1. Comparison of the proposed model with current state-of-the-art methods on the DHF1K benchmark [47]. The proposed model is more accurate (as measured by the official ranking metric AUC-J [4]) despite a model size reduction of 81% or more.

Sizable video saliency datasets have been available for some time [41], but only recently a dynamic model, ACLNet, was proposed that outperforms static models on a large-scale benchmark with diverse stimuli, DHF1K [47].

However, as methods for video saliency modeling progress, it is usually considered a separate task to image saliency prediction [1, 48, 19, 33, 28, 25] although the human visual system processes both coequally. Current dynamic models use image data only for pre-training [1, 19, 33, 28, 25], or perform image saliency prediction as a subordinate auxiliary task [47]. In addition, some methods are incompatible with image inputs since they require optical flow [1, 25] or fixed-length video frame sequence inputs for spatio-temporal convolutions [19, 33]. In this paper, we ask the question: *Is it possible to model static and dynamic saliency via one unified framework, with mutual benefit?*

We present preliminary experiments where we identify the domain shift between image and video saliency data and between different video saliency datasets as a crucial hurdle for joint modelling. We address this by proposing suitable domain adaptation techniques for the identified sources of domain shift. To study the benefit of the domain adaptation techniques, we propose the UNISAL neural network architecture, which is designed to model visual saliency on image and video data coequally while aiming for simplicity and low computational complexity. The network is simultaneously trained on three video datasets—DHF1K [47], Hollywood-2 and UCF-Sports [41]—and one image saliency dataset, SALICON [20].

We evaluate our method on the four training datasets, among which DHF1K and SALICON have held-out test sets. In addition, we evaluate on the established MIT300 image saliency benchmark [21]. We find that our model significantly outperforms current state-of-the-art methods on all video saliency datasets and achieves competitive performance for image saliency prediction, with a fraction of the model size and faster

runtime than competing models. The performance of UNISAL on the challenging DHF1K benchmark is shown in Figure 1.

In summary, our contributions are as follows:

- To the best of our knowledge, we make the first attempt to model image and video visual saliency with one unified framework.
- We identify different sources of domain shift as the main challenge for joint image and video saliency modeling and propose four novel domain adaptation techniques to enable strong shared features: Domain-Adaptive Priors, Domain-Adaptive Fusion, Domain-Adaptive Smoothing, and Bypass-RNN.
- Our method achieves state-of-the-art performance on all video saliency datasets and is on par with the state-of-the-art for all image saliency datasets. At the same time, the model achieves a 5 to 20-fold reduction in model size and faster runtime compared to all existing deep saliency models.

2 Related Work

2.1 Image Saliency Modeling

Most visual saliency modeling literature uses computational models to imitate human visual attention mechanisms on static scenes. Itti *et al.* [17] propose a first computational method to model visual saliency of images, and subsequent early saliency models [3, 42, 13, 26, 22] similarly focus on low-level image features such as intensity/contrast, color, edges, *etc.* These methods are therefore referred to as *bottom-up* methods. Recently, the field has achieved significant performance gains through deep neural networks since their powerful learning ability allows them to capture high-level, *top-down* features. Vig *et al.* [45] propose a data-driven approach by combining a neural network with a linear classifier. Jiang *et al.* [20] collect a large-scale human visual attention dataset, SALICON, to facilitate the exploration of deep learning-based saliency modeling. Thereafter, visual saliency modeling entered the deep learning era and papers mainly focus on network design. For instance, Pan *et al.* [35] propose shallow and deep CNNs for saliency prediction, and Wang *et al.* [46] present a skip layer structure that is designed to leverage the global and local information. Zheng *et al.* [50] investigate the impact of high-level observer tasks on saliency modeling. Although promising results have been achieved and exploration is still ongoing for image saliency modeling, dynamic scenes are arguably more relevant to human visual experience, but have received less attention in the literature to date.

2.2 Video Saliency Modeling

Similar to the image saliency models, early dynamic models for video saliency prediction [32, 31, 37, 15] are mainly based on low-level visual statistics, with additional temporal features (*e.g.*, optical flow). Marat *et al.* [32] extract frame pairs from video streams in order to compute a static and a dynamic saliency map accordingly, which are fused for the final prediction. By extending the center-surround saliency in static scenes, Mahadevan *et al.* [31] use dynamic textures to model video saliency. Zhong *et al.* [51]

combine spatial and temporal saliency features and fuse the predictions. The performance of these early models is limited by the representation ability of the low-level features for temporal information. Consequently, deep learning based methods have been introduced for dynamic saliency modeling in recent years. Gorji *et al.* [10] propose to incorporate attentional push for video saliency prediction, via a multi-stream convolutional long short-term memory network (ConvLSTM). Jiang *et al.* [19] show that human attention is easily attracted to moving objects and propose a saliency-structured ConvLSTM to generate video saliency. A recent work [48] presents a new large-scale dataset, DHF1K, for human fixation prediction in videos, and propose an attention mechanism with ConvLSTM to achieve better performance than static deep models. The DHF1K dataset, in turn, sparked advances [33, 25, 28] in video saliency prediction, exploring different strategies to extract temporal features (optical flow, 3D convolutions, different recurrences). However, the above methods either extend prior image saliency models or focus on video data alone, resulting in limited applicability to static scenes.

2.3 Spatio-Temporal Visual Prediction

Static visual prediction is usually seen as an instance of—and as a baseline for—dynamic visual prediction. However, very few papers in the literature consider both static and dynamic information in a unified model. Some methods [7, 23, 36, 39, 49, 24, 29, 44] are spatio-temporal but focus on leveraging spatial information to assist temporal prediction. Usually, however, these models are applicable to temporal data only. Dollár *et al.* [7] extend techniques used in image object recognition to the temporal domain. A 3D gradient based spatio-temporal descriptor for video sequences is introduced by Klaser *et al.* [23]. Kratz *et al.* [24] propose to use spatio-temporal motion patterns for anomaly detection in crowded scenes. Recent learning-based approaches [29] extend the image domain to the spatio-temporal domain by using LSTMs. Guo *et al.* [11] present a spatio-temporal model that predicts saliency on images and videos through the phase spectrum of the Quaternion Fourier Transform. This model, however relies on low-level hand-crafted features and cannot extract the high-level information that is necessary for accurate saliency prediction. Moreover, most existing spatio-temporal visual prediction model are specialized for video data, rendering the models unable to simultaneously model image saliency. Finally, domain-specific batch normalization has been explored to model the domain shift between different domains of the same type of data [5] (images), but not to model visual saliency or the domain-shift between different types of data (images and videos).

3 Unified Image and Video Saliency Modeling

3.1 Domain-Shift Modeling

In this section we present preliminary analyses to examine the domain shift among different image and video saliency dataset, and use the insights to design corresponding domain adaptation methods. Following Wang *et al.* [48], we select the video saliency datasets DHF1K [48], Hollywood-2 and UCF Sports [41], and the image saliency dataset SALICON [20].

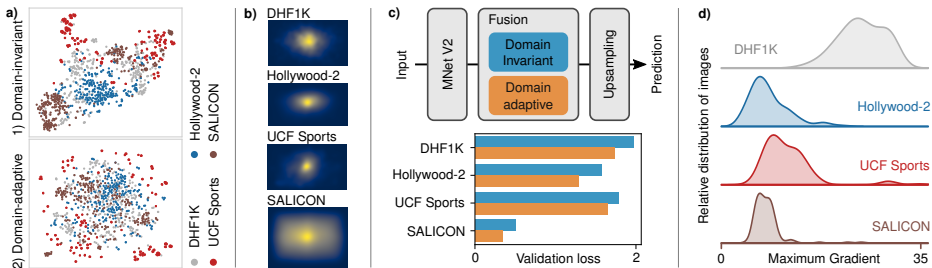


Fig. 2. Preliminary experiments to examine the domain shift between the training datasets. **a)** t-SNE visualization of MNNet V2 features after domain-invariant and domain-adaptive normalization. **b)** Average ground truth saliency maps of the training datasets. **c)** Comparison of validation losses when training a simplified saliency model with domain-invariant and domain-adaptive fusion. **d)** Distribution of ground truth saliency map sharpness after resizing to the model input distribution, measured by the maximum image gradients, for each training dataset.

Domain-Adaptive Batch Normalization. Batch normalization (BN) aims to reduce the internal covariate shift of neural network activations by transforming their distribution to zero mean and unit variance for each training batch. Simultaneously, it computes running estimates of the mean and variance for inference. However, estimating the statistics across different domains results in inaccurate intra-domain statistics, and therefore a performance trade-off. In order to examine the domain shift among the training datasets, we conduct a simple experiment: We randomly sample 256 images/frames from each dataset and compute their respective average pooled MobileNet V2 (MNNet V2) features. We then compute the t-SNE [30] of all feature vectors after normalizing each feature with the means and variances of 1) all samples (domain-invariant) or 2) the samples from the respective dataset (domain-adaptive). The results, shown in Figure 2 a), reveal a significant domain shift among the different datasets, which is mitigated by the domain-adaptive normalization. Following this observation, we use *Domain-Adaptive Batch Normalization (DABN)*, *i.e.*, a different set of BN modules for each dataset. During training and inference, each batch is constructed with data from one dataset and passed through the corresponding modules.

Domain-Adaptive Priors. Figure 2 b) shows the average ground truth saliency map for each training dataset. Among the video datasets, Hollywood-2 and UCF Sports exhibit the strongest center bias, which is plausible since they are biased towards certain content (movies and sports) while DHF1K is more diverse. SALICON has a much weaker center bias than the video saliency datasets, which can potentially be explained by the longer viewing time of each image/frame (5 s vs. 30 ms to 42 ms) that allows secondary stimuli to be fixated. Accordingly, we propose to learn a separate set of Gaussian prior maps for each dataset.

Domain-Adaptive Fusion. We hypothesize that similar visual stimuli can attract different amounts of visual attention across the training datasets. For example, the Hollywood-2 and UCF Sports datasets are *task-driven*, *i.e.*, the viewer is instructed to identify the

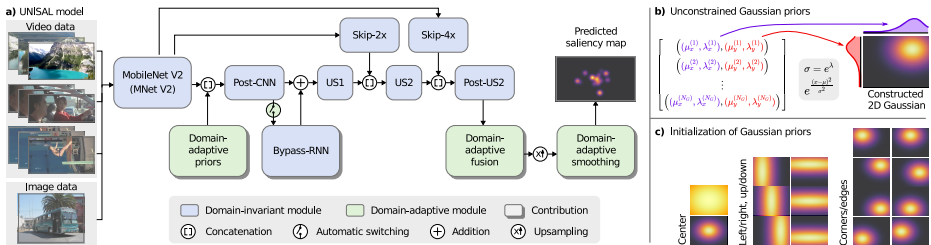


Fig. 3. **a)** Overview of the proposed framework. The model consists of a MobileNet V2 (MNet V2) encoder, followed by concatenation with learned Gaussian prior maps, a *Bypass-RNN*, a decoder network with skip connections, and *Fusion* and *Smoothing* layers. (see Section 3.2 and Table 1). The prior maps, fusion, smoothing and batch-normalization modules are domain-adaptive in order to account for domain-shift between the image and video saliency datasets and enable high-quality shared features (see Section 3.1). **b)** Construction of the prior maps from learned Gaussian parameters. Parameter maps provides a compact representation that is independent of the image resolution. **c)** Prior maps corresponding to the parameters at initialization.

main action shown. On the other hand, the DHF1K dataset contains *free-viewing* fixations. In order to test the hypothesis, we design a simplified saliency predictor (illustrated in Figure 2 c): The outputs of the MNet V2 model are fused to a single map by a *Fusion* layer (1×1 convolution) and upsampled through bilinear interpolation. We train the *Fusion* layer until convergence with 1) the same weights for all datasets (domain-invariant) or 2) different weights for each dataset (domain-adaptive). We find that the validation loss is lower for all datasets with setting 2), where the network can weigh the importance of the feature maps differently for each dataset. Consequently, we propose to learn a different set of *Fusion* layer weights for each dataset.

Domain-Adaptive Smoothing. The size of the blurring filter which is used to generate the ground truth saliency maps from the fixation maps can vary among datasets, especially since the images/frames are resized by different amounts for training. To examine this effect, we compute the distribution of the ground truth saliency map sharpness for each dataset. Here, we compute sharpness via the maximum image gradient magnitude after resizing the saliency map to the model input resolution. The results in Figure 2 d) confirm the heterogeneous distributions across datasets, revealing the highest sharpness for DHF1K. Therefore, we propose to blur the network output with a different learned *Smoothing* kernel for each dataset.

3.2 UNISAL Network Architecture

To study the benefit of the proposed domain-adaptation techniques, we introduce a simple and lightweight neural network architecture termed *UNISAL* that is designed to model image and video saliency coequally. The architecture, illustrated in Figure 3, follows an encoder-RNN-decoder design tailored for the saliency modeling task.

Encoder Network. We use the MobileNet-V2 (MNet V2) [38] as our backbone encoder for three reasons: First, its small memory footprint enables training with sufficiently large sequence length and batch size; second, its small number of floating point operations allows for real time inference; and third, we expect the relatively small number of parameters to mitigate overfitting on smaller datasets like UCF Sports. The main building blocks of MNet V2 are *inverted residuals*, i.e., sequences of pointwise convolutions that decompress and compress the feature space, interleaved with depthwise separable 3×3 convolutions. Overall, for an input resolution of $[r_x, r_y]$, MNet V2 computes feature maps at resolutions of $\frac{1}{2^\alpha} [r_x, r_y]$ with $\alpha \in \{1, 2, 3, 4, 5\}$. The output has 1280 channels and scale $\alpha = 5$. Domain-Adaptive Batch Normalization is not used in the MNet V2 since we initialize it with ImageNet-pretrained parameters.

Gaussian Prior Maps. The domain-adaptive Gaussian prior maps are constructed at runtime from learned means and standard deviations. The map with index $i = 1, \dots, N_G$ is computed as

$$g^{(i)}(x, y) = \gamma \exp \left(-\frac{(x - \mu_x^{(i)})^2}{(\sigma_x^{(i)})^2} - \frac{(y - \mu_y^{(i)})^2}{(\sigma_y^{(i)})^2} \right), \quad (1)$$

where γ is a scaling factor that is set to $\gamma = 6$ since the maps are concatenated with the ReLU6 activations of the MNet V2 output. In this formulation, if each standard deviation $\sigma_{xy}^{(i)}$ is optimized over \mathbb{R} , then the resulting variance $(\sigma_{xy}^{(i)})^2$ has the domain $\mathbb{R}_{\geq 0}$, which can lead to division by zero. Prior work which uses non-adaptive prior maps [6] addresses this by clipping $\sigma_{xy}^{(i)}$ to a predefined interval $[a, b]$ with $a > 0$ and clipping $\mu_{xy}^{(i)}$ to an interval around the center of the map. However, these constraints potentially limit the ability to learn the optimal parameters. Here, we propose *unconstrained Gaussian prior maps* by substituting $\sigma_{xy}^{(i)} = e^{\lambda_{xy}^{(i)}}$ and optimizing $\lambda_{xy}^{(i)}$ and $\mu_{xy}^{(i)}$ over \mathbb{R} . Moreover, instead of drawing the initial Gaussian parameters from a normal distribution, which results in highly correlated maps, we initialize $N_G = 16$ maps as shown in Figure 3 c), covering a broad range of priors. Finally, previous work usually introduces prior maps at the second to last layer in order to model the static center bias. Here, we concatenate the prior maps with the encoder output before the RNN and decoder, in order to leverage the prior maps in higher-level features.

Bypass-RNN. Modeling video saliency data requires a strategy to extract temporal features, such as an RNN, optical flow or 3D convolutions. However, none of these techniques are generally suitable to process static inputs, whereas our goal is to process images and videos with one model. Therefore, we introduce a *Bypass-RNN*, i.e., a RNN whose output is added to its input features via a residual connection that is automatically omitted (bypassed) for static batches during training and inference. Thus, the RNN only models the residual variations in visual saliency that are caused by temporal features.

In the UNISAL model, the *Bypass-RNN* is preceded by a *post-CNN* module, which compresses the concatenated MNet V2 outputs and Gaussian prior maps to 256 channels. For the Bypass-RNN, we use a convolutional GRU (*cGRU*) RNN [43] due to its relative simplicity, followed by a pointwise convolution. The cGRU has 256 hidden channels, 3×3 kernel size, recurrent dropout [9] with probability $p = 0.2$, and

MobileNet-style convolutions, *i.e.*, depthwise separable convolutions followed by pointwise convolutions.

Table 1. Network modules and corresponding operations. $ConvDW(c)$ denotes a depthwise separable convolution with c channels and kernel size 3×3 , followed by batch normalization and ReLU6 activation. $ConvPW(c_{in}, c_{out})$ is a pointwise 1×1 convolution with c_{in} input and c_{out} output channels, followed by batch normalization and, if $c_{in} \leq c_{out}$, by ReLU6 activation. $DO(p)$ denotes 2D dropout with probability p . $Up(c, n)$ denotes n -fold upsampling with bilinear interpolation of feature maps with c channels.

Module	Operations
Post-CNN	$ConvDW(1280)$, $ConvPW(1280, 256)$
Skip-4x	$ConvPW(64, 128)$, $DO(0.6)$, $ConvPW(128, 64)$
Skip-2x	$ConvPW(160, 256)$, $DO(0.6)$, $ConvPW(256, 128)$
US1	$Bilinear(256, 2)$
US2	$ConvPW(384, 768)$, $ConvDW(768)$, $ConvPW(768, 128)$, $Up(128, 2)$
Post-US2	$ConvPW(200, 400)$, $ConvDW(400)$, $ConvPW(400, 64)$
Fusion	$ConvPW(64, 1)$

Decoder Network and Smoothing. The details of the decoder modules are listed in Table 1. First, the Bypass RNN features are upsampled to scale $\alpha = 4$ by *US1* and concatenated with the output of *Skip-2x*. Next, the concatenated feature maps are upsampled to scale $\alpha = 3$ by *US2* and concatenated with the output of *Skip-4x*. The *Post-US2* features are reduced to a single channel by an *Domain-Adaptive Fusion* layer (1×1 convolution) and upsampled to the input resolution via nearest-neighbor interpolation. In visual saliency datasets, the ground truth saliency maps are usually generated by blurring the fixation maps with a predefined Gaussian filter [48]. Here, we equip the network with the ability to explicitly model this blurring operation by convolving the network output with a learned 41×41 *Smoothing* kernel. The upsampling is followed by a *Domain-Adaptive Smoothing* layer with 41×41 convolutional kernels that explicitly model the dataset-dependent blurring of the ground-truth saliency maps. Finally, following Jetley *et al.* [18], we transform the output into a generalized Bernoulli distribution by applying a softmax operation across all output values.

3.3 Domain-Aware Optimization

Domain-Adaptive Input Resolution. The images/frames of the training datasets each have different aspect ratios, specifically 4:3 for SALICON, 16:9 for DHF1K, and 1.85:1 (median) for Hollywood-2, and 3:2 (median) for UCF Sports. Our network architecture is fully-convolutional, and therefore agnostic to exact the input resolution. Moreover, each mini-batch is constructed from one dataset due to DABN. Therefore, we use input resolutions of 288×384 , 224×384 , 224×416 and 256×384 for SALICON, DHF1K, Hollywood-2 and UCF Sports, respectively.

Assimilated Frame Rate. The frame rate of the DHF1K videos is 30 fps compared to 24 fps for Hollywood-2 and UCF Sports. In order to assimilate the frame rates during training, and to train on longer time intervals, we construct clips using every 5th frame for DHF1K and every 4th frame for all others, yielding 6 fps overall. During inference, the same procedure is used and the predictions are interleaved.

4 Experiments

In this section, we evaluate the proposed method through extensive experiments and compare with current state-of-the-art methods. Detailed analyses are presented to gain an understanding of the proposed approach.

4.1 Experimental Setup

Datasets and Evaluation Metrics. In order to evaluate our proposed unified image and video saliency modeling framework, we jointly train the UNISAL model on datasets from both modalities. For fair comparison, we use the same training data as [47], i.e., the SALICON [20] image saliency dataset and the Hollywood-2 [41], UCF Sports [41], and DHF1K [47] video saliency datasets. For SALICON, we use the official training/validation/testing split of 10,000/5,000/5,000. For Hollywood-2 and UCF Sports, we use the training and testing splits of 823/884 and 103/47 videos, and the corresponding validation sets are randomly sampled 10% from the training sets, following [47]. For Hollywood-2, the videos are divided into individual shots. For the DHF1K dataset, we use the official training/validation/testing splits of 600/100/300 videos. The proposed approach is evaluated on the testing sets of the above-mentioned four datasets, with comparison to state-of-the-art methods. Moreover, we benchmark our model on the MIT300 benchmark [21], after fine-tuning on the MIT1003 dataset as suggested by the benchmark authors. As in prior work [3, 47], we use the evaluation metrics AUC-Judd (AUC-J), Similarity Metric (SIM), shuffled AUC (s-AUC), Linear Correlation Coefficient (CC), and Normalized Scanpath Saliency (NSS) [4]. Larger values indicate better performance.

Implementation Details. We optimize the network via Stochastic Gradient Descent with momentum of 0.9 and weight decay of 10^{-4} . Gradients are clipped to ± 2 . The learning rate is set to 0.04 and exponentially decayed by a factor of 0.8 after each epoch. The batch size is set to 4 for video data and 32 for SALICON. The video clip length is set to 12 frames that are sampled as described in Section 3.3. Videos that are too short are discarded for training, which applies to Hollywood-2. For comparability, we use the same loss formulation as Wang *et al.* [48]. The model is trained for 16 epochs and with early stopping on the DHF1K validation set. To prevent overfitting, the weights of MNet V2 are frozen for the first two epochs and afterwards trained with a learning rate that is reduced by a factor of 10. The pretrained BN statistics of MNet V2 are frozen throughout training. To account for dataset imbalance, the learning rate for SALICON is reduced by a factor of 2. Our model is implemented using the PyTorch framework and trained on a NVIDIA GTX 1080 Ti GPU. The code is available at <https://github.com/rdroste/unisal>.

Table 2. Quantitative performance on the video saliency datasets of DHF1K, Hollywood-2 and UCF Sports. The training settings (i) to (vi) denote training with: (i) DHF1K, (ii) Hollywood-2, (iii) UCF Sports, (iv) SALICON, (v) DHF1K+Hollywood-2+UCF Sports, and (vi) DHF1K+Hollywood-2+UCF Sports+SALICON. Best performance is shown in **bold** while the second best is underlined. The * symbol denotes training under setting (vi), while † indicates that the method is fine-tuned for each dataset.

Method \ Dataset	DHF1K					Hollywood-2					UCF Sports					
	AUC-J	SIM	s-AUC	CC	NSS	AUC-J	SIM	s-AUC	CC	NSS	AUC-J	SIM	s-AUC	CC	NSS	
Dynamic models	PQFT [12]	0.699	0.139	0.562	0.137	0.749	0.723	0.201	0.621	0.153	0.755	0.825	0.250	0.722	0.338	1.780
	Seo <i>et al.</i> [40]	0.635	0.142	0.499	0.070	0.334	0.652	0.155	0.530	0.076	0.346	0.831	0.308	0.666	0.336	1.690
	Rudoy <i>et al.</i> [37]	0.769	0.214	0.501	0.285	1.498	0.783	0.315	0.536	0.302	1.570	0.763	0.271	0.637	0.344	1.619
	Hou <i>et al.</i> [15]	0.726	0.167	0.545	0.150	0.847	0.731	0.202	0.580	0.146	0.684	0.819	0.276	0.674	0.292	1.399
	Fang <i>et al.</i> [8]	0.819	0.198	0.537	0.273	1.539	0.859	0.272	0.659	0.358	1.667	0.845	0.307	0.674	0.395	1.787
	OBDL [14]	0.638	0.171	0.500	0.117	0.495	0.640	0.170	0.541	0.106	0.462	0.759	0.193	0.634	0.234	1.382
	AWS-D [27]	0.703	0.157	0.513	0.174	0.940	0.694	0.175	0.637	0.146	0.742	0.823	0.228	0.750	0.306	1.631
	OM-CNN [19]	0.856	0.256	0.583	0.344	1.911	0.887	0.356	0.693	0.446	2.313	0.870	0.321	0.691	0.405	2.089
	Two-stream [1]	0.834	0.197	0.581	0.325	1.632	0.863	0.276	0.710	0.382	1.748	0.832	0.264	0.685	0.343	1.753
	*ACLNet [48]	0.890	0.315	0.601	0.434	2.354	0.913	<u>0.542</u>	0.757	0.623	3.086	0.897	0.406	0.744	0.510	2.567
	TASED-Net [33]	0.895	0.361	0.712	0.470	2.667	0.918	0.507	0.768	0.646	3.302	0.899	0.469	0.752	0.582	2.920
	STRA-Net [25]	0.895	0.355	0.663	0.458	2.558	0.923	0.536	<u>0.774</u>	0.662	3.478	0.910	0.479	0.751	0.593	3.018
†SaLEMA [28]	0.890	0.465	0.667	0.449	2.573	0.919	0.487	0.708	0.613	3.186	0.906	0.431	0.740	0.544	2.638	
*SaLEMA [28]	0.895	0.283	0.739	0.414	2.285	0.875	0.371	0.663	0.456	2.214	0.899	0.381	0.769	0.521	2.503	
Static models	ITTI [17]	0.774	0.162	0.553	0.233	1.207	0.788	0.221	0.607	0.257	1.076	0.847	0.251	0.725	0.356	1.640
	GBVS [13]	0.828	0.186	0.554	0.283	1.474	0.837	0.257	0.633	0.308	1.336	0.859	0.274	0.697	0.396	1.818
	SALICON [16]	0.857	0.232	0.590	0.327	1.901	0.586	0.321	0.711	0.425	2.013	0.848	0.304	0.738	0.375	1.838
	Shallow-Net [35]	0.833	0.182	0.529	0.295	1.509	0.851	0.276	0.694	0.423	1.680	0.846	0.276	0.691	0.382	1.789
	Deep-Net [35]	0.855	0.201	0.592	0.331	1.775	0.884	0.300	0.736	0.451	2.066	0.861	0.282	0.719	0.414	1.903
	*Deep-Net [35]	0.874	0.288	0.610	0.374	1.983	0.901	0.482	0.740	0.597	2.834	0.880	0.365	0.729	0.475	2.448
	DVA [46]	0.860	0.262	0.595	0.358	2.013	0.886	0.372	0.727	0.482	2.459	0.872	0.339	0.725	0.439	2.311
	*DVA [46]	0.883	0.297	0.623	0.397	2.237	0.907	0.497	0.753	0.607	2.942	0.892	0.387	0.740	0.492	2.503
SalGAN [34]	0.866	0.262	0.709	0.370	2.043	0.901	0.393	0.789	0.535	2.542	0.876	0.332	0.762	0.470	2.238	
UNISAL (ours)	Training setting (i)	<u>0.899</u>	0.378	0.686	0.481	2.707	0.920	0.496	0.710	0.612	3.279	0.896	0.443	0.717	0.553	2.689
	Training setting (ii)	0.881	0.313	0.690	0.422	2.352	<u>0.932</u>	0.534	0.762	0.672	3.803	0.892	0.440	0.735	0.566	2.768
	Training setting (iii)	0.869	0.286	0.664	0.375	2.056	0.890	0.392	0.683	0.475	2.350	0.908	0.502	0.764	0.614	3.076
	Training setting (iv)	0.883	0.288	<u>0.715</u>	0.410	2.259	0.912	0.432	0.750	0.565	2.897	0.892	0.428	<u>0.776</u>	0.561	2.740
	Training setting (v)	0.901	0.384	0.692	<u>0.488</u>	<u>2.739</u>	0.934	0.544	0.758	0.675	3.909	<u>0.917</u>	<u>0.514</u>	0.786	<u>0.642</u>	<u>3.260</u>
	Training setting (vi)	0.901	<u>0.390</u>	0.691	0.490	2.776	0.934	<u>0.542</u>	0.759	<u>0.673</u>	<u>3.901</u>	0.918	0.523	0.775	0.644	3.381

4.2 Quantitative Evaluation

The results of the quantitative evaluation are shown in Table 2 for the video saliency datasets and in Tables 3 and 4 for the image datasets. For video saliency prediction, in order to analyze the impact of—and generalization across—different datasets, we evaluate six training settings: i) DHF1K, ii) Hollywood-2, iii) UCF Sports, iv) SALICON, v) DHF1K, Hollywood-2, and UCF Sports, vi) DHF1K, Hollywood-2, UCF Sports and SALICON. For fair comparison, we include state-of-the-art methods that are trained on our best-performing training setting (iv): The ACLNet [48] video saliency model and the Deep-Net [35] and DVA [46] image saliency models. In addition, we provide the performance of SaLEMA [28], which is based on SalGAN [34], after fine-tuning the model in training setting (vi). Other state-of-the-art video saliency models [19, 33, 25] are not suitable for training with image data as discussed in Section 1. We observe that the proposed UNISAL model significantly outperforms previous static and dynamic methods, across almost all the metrics. We obtain the following additional findings:



Fig. 4. Qualitative performance of the proposed approach on video (top part) and image (bottom part) saliency prediction.

Table 3. Quantitative performance on the SALICON and MIT300 benchmarks. Best performance is shown in **bold** while the second best is underlined. Training setting (vi) is used for UNISAL.

Method \ Dataset	SALICON					MIT300				
	AUC-J	SIM	s-AUC	CC	NSS	AUC-J	SIM	s-AUC	CC	NSS
ITTI [17]	0.667	0.378	0.610	0.205	-	0.75	0.44	0.63	0.37	0.97
GBVS [13]	0.790	0.446	0.630	0.421	-	0.81	0.48	0.63	0.48	1.24
SALICON [16]	-	-	-	-	-	0.87	0.60	0.74	<u>0.74</u>	<u>2.12</u>
Shallow-Net [35]	<u>0.836</u>	<u>0.520</u>	0.670	0.596	-	0.80	0.46	0.64	0.53	-
Deep-Net [35]	-	-	0.724	0.609	1.859	0.83	0.52	0.69	0.58	1.51
DVA [46]	-	-	-	-	-	0.85	0.58	0.71	0.68	1.98
SalGAN [34]	-	-	0.772	<u>0.781</u>	2.459	<u>0.86</u>	<u>0.63</u>	<u>0.72</u>	0.73	2.04
UNISAL (ours)	0.864	0.775	<u>0.739</u>	0.879	<u>1.952</u>	0.872	0.674	0.743	0.784	2.322

Table 4. Quantitative comparison for dynamic models on the static SALICON benchmark. Best performance is shown in **bold** while the second best is underlined. Training setting (vi) is used for all methods.

Method	AUC-J	SIM	s-AUC	CC	NSS
SalEMA [28]	0.732	0.470	0.519	0.411	0.760
ACLNet [48]	0.843	0.688	<u>0.698</u>	0.771	1.618
UNISAL (w/o DA)	<u>0.848</u>	<u>0.690</u>	0.676	<u>0.799</u>	<u>1.654</u>
UNISAL (final)	0.864	0.775	0.739	0.879	1.952

1) Training with all video saliency datasets (setting (v)) *always* improves performance compared to individual video saliency datasets (settings (i) to (iii)). This has not been the case for UCF Sports in a previous cross-dataset evaluation study [48]. 2) Additionally including image saliency data (setting (vi)) further improves performance for most metrics for DHF1K and UCF Sports. The exception is Hollywood-2, but the performance decrease is less than 1%.

For image saliency prediction, UNISAL performs on par with state-of-the-art image saliency models both on the SALICON and MIT300 benchmark as shown in Table 3. In addition, we evaluate state-of-the-art video saliency models on SALICON dataset as shown in Table 4. For ACLNet [48] we use the auxiliary output which is trained on SALICON (using the LSTM output yielded worse performance). For SalEMA [28], we fine-tuned their best performing model with training setting (vi). A large performance jump can be observed for the domain-adaptive UNISAL model.

4.3 Qualitative Evaluation

In Figure 4, we show randomly selected saliency predictions for both images and videos. It is visible that the proposed unified model performs well on both modalities. For challenging dynamic scenes with complete occlusion (DHF1K, left), the model correctly

memorizes the salient object location, indicating that long-term temporal dependencies are effectively modeled. Moreover, the model correctly predicts shifting observer focus in the presence of multiple salient objects, as evident from the Hollywood-2 and UCF Sports samples. The results on static scenes (bottom part of Figure 4) confirm that the proposed unified model indeed generalizes to static scenes.

Table 5. Ablation study of the proposed approach on the DHF1K and SALICON validation sets. The proposed components are added incrementally to the baseline to quantify their contribution. Training setting (vi) is used for this study.

Dataset Config.	DHF1K					SALICON				
	KLD ↓	AUC-J ↑	SIM ↑	CC ↑	NSS ↑	KLD ↓	AUC-J ↑	SIM ↑	CC ↑	NSS ↑
Baseline	1.877	0.863	0.282	0.372	2.057	0.551	0.824	0.607	0.711	1.415
+ Gaussian	1.776	0.879	0.300	0.411	2.273	0.394	0.848	0.675	0.801	1.634
+ RNNRes	1.754	0.881	0.302	0.411	2.274	0.450	0.843	0.648	0.770	1.531
+ SkipConnect	1.749	0.884	0.308	0.412	2.301	0.404	0.841	0.673	0.777	1.600
+ Smoothing	1.770	0.882	0.295	0.416	2.305	0.369	0.848	0.690	0.799	1.654
+ DomainAdaptive	1.526	0.907	0.373	0.482	2.731	0.231	0.867	0.768	0.877	1.925
Final	1.531	0.907	0.381	0.487	2.755	0.226	0.867	0.771	0.880	1.923

4.4 Ablation Study

We present an ablation study, analyzing the contribution of each proposed component: 1) Gaussian prior maps; 2) RNN residual connection; 3) skip connections; 4) *Smoothing* layer; 5) domain-adaptive operations (incl. Bypass-RNN); and 6) domain-aware optimization. We evaluate the performance of the above configurations on the representative DHF1K and SALICON validation sets. The results are listed in Table 5, including the KL-divergence (KLD) metric in addition to the aforementioned metrics. We find that each of the proposed components contributes a considerable performance increase. Overall, the domain-adaptive operations contribute the most, both for DHF1K and SALICON. This indicates that mitigating the domain shift between datasets is a crucial component of UNISAL, confirming our initial studies in Section 3.1. The Gaussian prior maps yield the second largest gain, indicating the effectiveness of our proposed unconstrained optimization of the Gaussian parameters and their early position in the model.

4.5 Inter-Dataset Domain Shift

Figure 5 shows analysis of the four domain-adaptive modules, *i.e.*, DABN, *Domain-Adaptive Fusion*, *Domain-Adaptive Priors* and *Domain-Adaptive Smoothing*. The DABN estimated means in Figure 5 a) are correlated between video datasets with Pearson correlation coefficients r between 82% to 83%, but not correlated between SALICON and

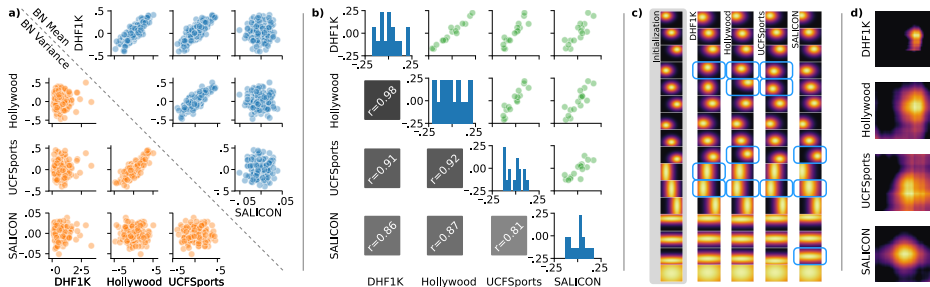


Fig. 5. Retrospective analysis of the domain-adaptive modules. a) Correlation of the batch normalization statistics between datasets (*US2* module, representative). The upper-right plots correlate the estimated means and the lower-left plots the estimated variances. b) Correlation of the *Fusion* layer weights between datasets. The plots on the diagonal show the distribution of weights of the respective dataset. The lower-left part shows Pearson’s correlation coefficients. c) Gaussian prior maps compared to initialization. Significant deviations from the initialization are highlighted. d) *Smoothing* kernel of each dataset.

the video datasets ($r < 3\%$). For the estimated variances, only Hollywood-2 and UCF Sports are correlated ($r = 82\%$). This confirms the shift of the feature distributions between datasets, especially between SALICON and the video data.

The domain-adaptive *Fusion* layer weights shown in Figure 5 b) are generally correlated across datasets, with $r > 81\%$. However, as for the DABN, SALICON is the least correlated with the other datasets. Moreover, many of the SALICON *Fusion* weights lie near zero compared to the video datasets, which indicates that only a subset of the video saliency features is relevant for image saliency. The *Domain-Adaptive Fusion* layer models these differences while the remaining network weights are shared.

The domain-adaptive Gaussian prior maps shown in Figure 5 c) are successfully learned with our proposed unconstrained parametrization, as observed by the deviations from the initialization. Some prior maps are similar across datasets while others vary visibly, indicating that the different domains have different optimal priors.

Finally, the learned *Smoothing* kernels shown in Figure 5 d) vary significantly across datasets. As expected, the DHF1K dataset, which has the least blurry training targets, results in the most narrow *Smoothing* filter.

4.6 Computational Load

With the design of ever more complex network architectures, few studies evaluate the model size, although performance gains can often be traced back to more parameters. We compare the size of UNISAL to the state-of-the-art video saliency predictors in the left column of Table 6. Our model is the most light-weight by a significant margin, with over $5\times$ smaller size than TASED-Net, which is the current state-of-the-art on the DHF1K benchmark (see also Figure 1). The same result applies when comparing to the deep image saliency methods from Table 3, whose sizes range from 92 MB for DVA to 2.5 GB for Shallow-Net.

Table 6. Model size and runtime comparison of video saliency prediction methods. Existing methods are reported based on the DHF1K benchmark [48]. Best performance is shown in **bold**.

Method	Model size (MB)	Method	Runtime (s)
Shallow-Net [35]	2,500	Two-stream [1]	20
STRA-Net [25]	641	SALICON [16]	0.5
SalEMA [28]	364	Shallow-Net [35]	0.1
Two-stream [1]	315	DVA [46]	0.1
ACLNet [48]	250	Deep-Net [35]	0.08
SalGAN [34]	130	TASED-Net [33]	0.06
SALICON [16]	117	ACLNet [48]	0.02
Deep-Net [35]	103	SalGAN [34]	0.02
DVA [46]	96	STRA-Net [25]	0.02
TASED-Net [33]	82	SalEMA [28]	0.01
UNISAL (ours)	15.5	UNISAL (ours)	0.009

Another key issue for real-world applications is the model efficiency. Consequently, we present a GPU runtime comparison (processing time per frame) of video saliency models in the right column of Table 6. Our model is the most efficient one compared to previous state-of-the-art methods. In addition, we observe a CPU (Intel Xeon W-2123 at 3.60GHz) runtime of 0.43 s (2.3 fps), which is faster than some models’ GPU runtime, which further demonstrates the applicability of the proposed framework. Considering both the model size and the runtime, the proposed saliency modeling approach achieves state-of-the-art performance in terms of real-world applicability.

5 Discussion and Conclusion

In this paper, we have presented a simple yet effective approach to unify static and dynamic saliency modeling. We found it crucial to account for different sources of the inter-dataset domain shift through corresponding novel domain-adaptive modules. We integrated the domain-adaptive modules into the new, lightweight and simple UNISAL architecture which is designed to model both data modalities coequally. We observed state-of-the-art performance on video saliency datasets, and competitive performance on image saliency datasets, with a 5 to 20-fold reduction in model size compared to the *smallest* previous deep model, and faster runtime. We found that due to the domain adaptation, joint training with all datasets improved the performance on each individual dataset overall. We presented preliminary and retrospective experiments which explain the merit of the domain-adaptive modules.

To our knowledge, this is the first attempt towards unifying image and video saliency modeling in a single framework. We believe that our work can serve as a basis for further research into joint modeling of these modalities.

References

1. Bak, C., Kocak, A., Erdem, E., Erdem, A.: Spatio-temporal saliency networks for dynamic saliency prediction. *IEEE TMM* **20**(7), 1688–1698 (2017)
2. Borji, A.: Saliency Prediction in the Deep Learning Era: An Empirical Investigation. arXiv:1810.03716 (2018)
3. Borji, A., Itti, L.: State-of-the-art in visual attention modeling. *IEEE TPAMI* **35**(1), 185–207 (2012)
4. Bylinskii, Z., Judd, T., Oliva, A., Torralba, A., Durand, F.: What Do Different Evaluation Metrics Tell Us About Saliency Models? *IEEE TPAMI* **41**(3), 740–757 (2019).
5. Chang, W.G., You, T., Seo, S., Kwak, S., Han, B.: Domain-specific batch normalization for unsupervised domain adaptation. In: *CVPR* (2019)
6. Cornia, M., Baraldi, L., Serra, G., Cucchiara, R.: Predicting Human Eye Fixations via an LSTM-based Saliency Attentive Model. *IEEE TIP* **27**(10), 5142–5154 (2016).
7. Dollár, P., Rabaud, V., Cottrell, G., Belongie, S.: Behavior recognition via sparse spatio-temporal features (2005)
8. Fang, Y., Wang, Z., Lin, W., Fang, Z.: Video saliency incorporating spatiotemporal cues and uncertainty weighting. *IEEE TIP* **23**(9), 3910–3921 (2014)
9. Gal, Y., Ghahramani, Z.: A Theoretically Grounded Application of Dropout in Recurrent Neural Networks. In: *NeurIPS* (2016).
10. Gorji, S., Clark, J.J.: Going from image to video saliency: Augmenting image salience with dynamic attentional push. In: *CVPR* (2018)
11. Guo, C., Ma, Q., Zhang, L.: Spatio-temporal saliency detection using phase spectrum of quaternion fourier transform. In: *CVPR* (2008)
12. Guo, C., Zhang, L.: A novel multiresolution spatiotemporal saliency detection model and its applications in image and video compression. *IEEE TIP* **19**(1), 185–198 (2009)
13. Harel, J., Koch, C., Perona, P.: Graph-based visual saliency. In: *NeurIPS* (2007)
14. Hossein Khatoonabadi, S., Vasconcelos, N., Bajic, I.V., Shan, Y.: How many bits does it take for a stimulus to be salient? In: *CVPR* (2015)
15. Hou, X., Zhang, L.: Dynamic visual attention: Searching for coding length increments. In: *NeurIPS* (2009)
16. Huang, X., Shen, C., Boix, X., Zhao, Q.: Salicon: Reducing the semantic gap in saliency prediction by adapting deep neural networks. In: *ICCV* (2015)
17. Itti, L., Koch, C., Niebur, E.: A model of saliency-based visual attention for rapid scene analysis. *IEEE TPAMI* (11), 1254–1259 (1998)
18. Jetley, S., Murray, N., Vig, E.: End-to-End Saliency Mapping via Probability Distribution Prediction. In: *CVPR* (2016).
19. Jiang, L., Xu, M., Liu, T., Qiao, M., Wang, Z.: DeepVS: A Deep Learning Based Video Saliency Prediction Approach. In: *ECCV* (2018).
20. Jiang, M., Huang, S., Duan, J., Zhao, Q.: Salicon: Saliency in context. In: *CVPR* (2015)
21. Judd, T., Durand, F., Torralba, A.: A Benchmark of Computational Models of Saliency to Predict Human Fixations. *Mit-Csail-Tr-2012* **1**, 1–7 (2012).
22. Judd, T., Ehinger, K., Durand, F., Torralba, A.: Learning to predict where humans look. In: *ICCV* (2009)
23. Klaser, A., Marszałek, M., Schmid, C.: A spatio-temporal descriptor based on 3d-gradients (2008)
24. Kratz, L., Nishino, K.: Anomaly detection in extremely crowded scenes using spatio-temporal motion pattern models. In: *CVPR* (2009)
25. Lai, Q., Wang, W., Sun, H., Shen, J.: Video saliency prediction using spatiotemporal residual attentive networks. *IEEE TIP* (2019)

26. Le Meur, O., Le Callet, P., Barba, D., Thoreau, D.: A coherent computational approach to model bottom-up visual attention. *IEEE TPAMI* **28**(5), 802–817 (2006)
27. Leboran, V., Garcia-Diaz, A., Fdez-Vidal, X.R., Pardo, X.M.: Dynamic whitening saliency. *IEEE TPAMI* **39**(5), 893–907 (2016)
28. Linardos, P., Mohedano, E., Nieto, J.J., McGuinness, K., Giro-i Nieto, X., O’Connor, N.E.: Simple vs complex temporal recurrences for video saliency prediction. In: *BMVC* (2019)
29. Liu, J., Shahroudy, A., Xu, D., Wang, G.: Spatio-temporal lstm with trust gates for 3d human action recognition. In: *ECCV* (2016)
30. Maaten, L.v.d., Hinton, G.: Visualizing data using t-sne. *Journal of machine learning research* **9**(Nov), 2579–2605 (2008)
31. Mahadevan, V., Vasconcelos, N.: Spatiotemporal saliency in dynamic scenes. *IEEE TPAMI* **32**(1), 171–177 (2009)
32. Marat, S., Phuoc, T.H., Granjon, L., Guyader, N., Pellerin, D., Guérin-Dugué, A.: Modelling spatio-temporal saliency to predict gaze direction for short videos. *International journal of computer vision* **82**(3), 231 (2009)
33. Min, K., Corso, J.J.: Tased-net: Temporally-aggregating spatial encoder-decoder network for video saliency detection. In: *ICCV* (2019)
34. Pan, J., Ferrer, C.C., McGuinness, K., O’Connor, N.E., Torres, J., Sayrol, E., Giro-i Nieto, X.: Salgan: Visual saliency prediction with generative adversarial networks. *arXiv preprint arXiv:1701.01081* (2017)
35. Pan, J., Sayrol, E., Giro-i Nieto, X., McGuinness, K., O’Connor, N.E.: Shallow and deep convolutional networks for saliency prediction. In: *CVPR* (2016)
36. Rodriguez, M.D., Ahmed, J., Shah, M.: Action mach a spatio-temporal maximum average correlation height filter for action recognition. In: *CVPR* (2008)
37. Rudoy, D., Goldman, D.B., Shechtman, E., Zelnik-Manor, L.: Learning video saliency from human gaze using candidate selection. In: *CVPR* (2013)
38. Sandler, M., Howard, A., Zhu, M., Zhmoginov, A., Chen, L.C.: MobileNetV2: Inverted Residuals and Linear Bottlenecks. In: *CVPR* (2018)
39. Schuldt, C., Laptev, I., Caputo, B.: Recognizing human actions: a local svm approach. In: *ICPR* (2004)
40. Seo, H.J., Milanfar, P.: Static and space-time visual saliency detection by self-resemblance. *Journal of vision* **9**(12), 15–15 (2009)
41. Stefan Mathe, C.S.: Actions in the eye: Dynamic gaze datasets and learnt saliency models for visual recognition. *IEEE TPAMI* **37** (2015)
42. Sun, Y., Fisher, R.: Object-based visual attention for computer vision. *Artificial intelligence* **146**(1), 77–123 (2003)
43. Valipour, S., Siam, M., Jagersand, M., Ray, N.: Recurrent Fully Convolutional Networks for Video Segmentation. In: *WACV* (2017).
44. Varol, G., Laptev, I., Schmid, C.: Long-term temporal convolutions for action recognition. *IEEE TPAMI* **40**(6), 1510–1517 (2017)
45. Vig, E., Dorr, M., Cox, D.: Large-scale optimization of hierarchical features for saliency prediction in natural images. In: *CVPR* (2014)
46. Wang, W., Shen, J.: Deep visual attention prediction. *IEEE TIP* **27**(5), 2368–2378 (2017)
47. Wang, W., Shen, J., Guo, F., Cheng, M.M., Borji, A.: Revisiting video saliency: A large-scale benchmark and a new model. In: *CVPR* (2018)
48. Wang, W., Shen, J., Xie, J., Cheng, M.M., Ling, H., Borji, A.: Revisiting video saliency prediction in the deep learning era. *IEEE TPAMI* (2019)
49. Willems, G., Tuytelaars, T., Van Gool, L.: An efficient dense and scale-invariant spatio-temporal interest point detector. In: *ECCV* (2008)
50. Zheng, Q., Jiao, J., Cao, Y., Lau, R.W.: Task-driven webpage saliency. In: *ECCV* (2018)

51. Zhong, S.h., Liu, Y., Ren, F., Zhang, J., Ren, T.: Video saliency detection via dynamic consistent spatio-temporal attention modelling. In: AAAI (2013)